ACS APPLIED MATERIALS & INTERFACES

www.acsami.org

Research Article

BioMOF@PAN Mixed Matrix Membranes as Fast and Efficient Adsorbing Materials for Multiple Heavy Metals' Removal

Paula Escamilla,[#] Marcello Monteleone,[#] Rita Maria Percoco, Teresa F. Mastropietro,* Mariagiulia Longo, Elisa Esposito, Alessio Fuoco, Johannes C. Jansen,* Rosangela Elliani, Antonio Tagarelli, Jesus Ferrando-Soria, Valeria Amendola, Emilio Pardo,* and Donatella Armentano*

Cite This: *ACS Appl. Mater. Interfaces* 2024, 16, 51182–51194

Read Online

ACCESS | Metrics & More | Article Recommendations | Supporting Information

ABSTRACT: Heavy metal ions are a common source of water pollution. In this study, two novel membranes with biobased metal−organic frameworks (BioMOFs) embedded in a polyacrylonitrile matrix with tailored porosity were prepared via nonsolvent induced phase separation methods and designed to efficiently adsorb heavy metal ions from oligomineral water. Under optimized preparation conditions, stable membranes with high MOF loading up to 50 wt % and a cocontinuous sponge-like morphology and a high water permeability of 50−60 L m^{-2} h^{-1} bar^{-1} were obtained. The tortuous flow path in combination with a low water flow rate guarantees maximum contact time between the fluid and the MOFs, and thus a high heavy metal capture efficiency in a single pass. The performances of these BioMOF@PAN membranes were investigated in the dynamic regime for the simultaneous removal of Pb^{2+}, Cd^{2+}, and Hg^{2+} heavy metals from aqueous environments in the presence of common interfering ions. The new composite adsorbing membranes are capable of reducing the concentration of heavy metal pollutants in a single pass and at much higher efficiency than previously reported membranes. The enhanced performance of the mixed matrix membranes is attributed to the presence of multiple recognition sites which densely decorate the BioMOF channels: (i) the thioether groups, deriving from the *S*-methyl-L-cysteine and (*S*)-methionine amino acid residues, able to recognize and capture Pb^{2+} and Hg^{2+} ions and (ii) the oxygen atoms of the oxamate moieties, which preferentially interact with Cd^{2+} ions, as revealed by single crystal X-ray diffraction. The flexibility of the pore environments allows these sites to work synergically for the simultaneous capture of different metal ions. The stability of the membranes for a potential regeneration process, a key-factor for the effective feasibility of the process in real life applications, was also evaluated and confirmed less than 1% capacity loss in each cycle.

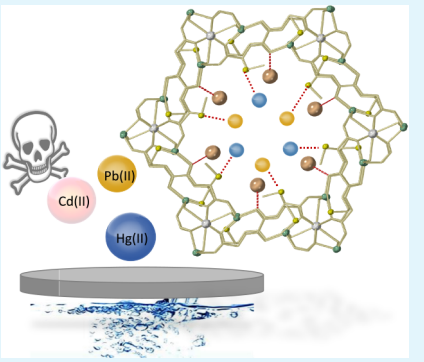

KEYWORDS: *metal−organic frameworks, polymeric membranes, heavy metals, adsorption, water treatment*

INTRODUCTION

Contamination of aquatic environments due to anthropogenic activities, urbanization, industrialization, and natural resource exploitation constitutes a global issue of increasing concern for our modern society.[1−3] The continuous uncontrolled release of micropollutants into the environment may cause undesirable effects on ecosystems and human health due to combined long-range transport, accumulation, persistence, and long-exposure effects.[4] Conventional urban wastewater treatment plants are not originally designed to remove all these types of contaminants, and the search for new and more advanced water treatment solutions has become of paramount importance to reduce their disposal.[5,6]

Since aquatic systems are crucial for the preservation of all ecosystems and for the production of drinking water, surface water needs to be protected, through monitoring programs, risk assessment, and mitigation measures. In this regard, a framework for EU action in the field of water policy was established by Directive 2000/60/EC (2000).[7] A complete Watch List of priority substances/group of substances (PSs) that should be monitored has been published in Decision 2015/495/EU (2015),[8] aiming at achieving a safe ecological and chemical level of surface water and groundwater bodies. The current PSs include a range of industrial chemicals, plant protection products, and metals/metal derivatives such as cadmium, mercury, nickel, and lead. Because of their persistence, bioaccumulation and/or toxicity,[9−11] these metals have also been identified as priority hazardous substances (PHSs), consistently with the criteria for substances of very high concern (SVHCs) under REACH.[12]

Unlike the situation with organic pollutants, which can be treated with advanced chemical/oxidation technologies,[13]

Received: July 24, 2024
Revised: September 2, 2024
Accepted: September 3, 2024
Published: September 13, 2024

including light-driven processes,[14] the removal of heavy metals requires, on a mandatory basis, their physical removal. Existing capture methods include precipitation, coagulation/flocculation, membrane technology, and adsorption by porous materials.[15−20] However, these currently available technologies, working separately, exhibit various shortcomings in terms of efficiency, selectivity, and, especially, processability and recyclability.[21] Moreover, successful much-needed novel methodologies should be able to treat enormous volumes of liquid, allowing high fluxes at low pressure.

Membrane-based separation technology can play a key role in addressing the global challenges of water scarcity and the pollution of aquatic environments, and it has been increasingly applied in water purification processes.[22,23] However, the use of water purification membranes still constitutes a challenge due to the inherent limitations of customary membrane materials which do not allow fine control of the structure and properties of the selective layer.[24,25] Recently, adsorptive membranes have emerged as novel materials for application in advanced wastewater purification and desalination technologies, owing to their potential in overcoming the shortcomings of conventional membranes and the trade-off between membrane selectivity and permeability.[25−27] An easy and convenient approach to prepare adsorptive membranes with high productivity is incorporating nanomaterials or nanostructured adsorbents into the polymeric matrix.[28,29] Several inorganic and organic adsorbents featuring large surface area-to-volume ratio, high interfacial activity, and adsorption capacity have been designed for targeted applications and have been used as possible fillers in membranes covering the entire range of filtration. One of the challenges is the stable inclusion of the fillers into the membrane matrix to overcome at once the common handling problems, suspension stability, and agglomeration concerns associated with the powdered formulation and to impart the membrane with unique functionalities. Each type of process needs a membrane with a specific morphology (structure, average pore size, and pore-size distribution), which requires accurate control of the variables that determine the membrane formation process and yield defect-free membranes.[30]

Among the variety of potential fillers, metal−organic frameworks (MOFs)[31] have emerged as promising candidates for advanced membrane development, yielding the so-called mixed-matrix membrane MOFs (MMM-MOFs), due to their versatile architecture, regular pore size, and functional surface area.[32−35] As fillers, MOFs can improve both the adsorption capacity, and selectivity, as well as the membrane hydrophilicity and water permeability, by offering alternative diffusion pathways through their porous channels and at the MOF/polymer interface.

Within this context, we recently reported different MOFs, derived from natural amino acids, including those based on (*S*)-methyl-(*L*)-cysteine and (S)-methionine, with formulas $\{M^{II}Cu_6^{II}[(S,S)\text{-Mecysmox}]_3(OH)_2(H_2O)\}\cdot 12H_2O$[36,37] and $\{M^{II}Cu_6^{II}[(S,S)\text{-methox}]_3(OH)_2(H_2O)\}\cdot 16H_2O$[38−42] (where M^{II} = Ca or Sr, Mecysmox = bis[*S*-methyl-L-cysteine]-oxalyldiamide and methox= bis[(S)-methionine]-oxalyldiamide) (Scheme 1). These MOFs, featuring hexagonal channels densely decorated with thioether groups belonging to the amino acid residues, appeared as suitable candidates for water remediation. Indeed, these MOFs were capable of efficiently and selectively adsorbing organic molecules[40−42] and/or heavy metal cations.[38,39] In later works, both

Scheme 1. Chemical Structures of the Chiral (*) *S*-Methyl-L-Cysteine Methyl Ester and (*S*)-Methionine Methyl Ester (a and b, Respectively) and of the Bis(Amino Acid)Oxamidate Ligand (c)

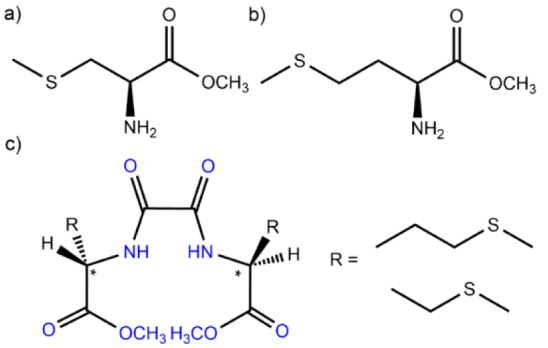

MOFs[37]—and also another multivariate MOF[43] (MTV-MOF) containing 50% of each amino acid—were integrated into Matrimid5218 polymeric films. The resulting MMM-MOFs exhibited excellent capacities in mercury and lead removal, respectively. In summary, this family of MOFs exhibited very good selectivity toward metal pollutants, which was preserved upon immobilization within the composite materials.

In this work, we report two novel MMM-MOFs, containing two water-stable, robust, and eco-friendly isoreticular Zn(II)-based BioMOFs with formulas $\{Ca^{II}Zn^{II}_6[(S,S)\text{-Mecysmox}]_3(OH)_2(H_2O)\}\cdot 12H_2O$ (**1**)[44,45] and the novel $\{Ca^{II}Zn^{II}_6[(S,S)\text{-Methox}]_3(OH)_2(H_2O)\}\cdot 16H_2O$ (**2**) as adsorbing fillers, and with polyacrylonitrile (PAN) as the polymeric matrix. While our previously reported Matrimid polyimide membranes required multiple passes to reach moderate Hg^{2+} capture efficiency, here we present a radically improved BioMOF@PAN MMM system with a tortuous flow path and high MOF loading with very high adsorption efficiency even in a single pass. The chemical−physical properties and the performance of these BioMOF@PAN MMMs for the simultaneous removal of Pb^{2+}, Cd^{2+}, and Hg^{2+} from aqueous environments, in the presence of common interfering ions, will be discussed.

MATERIALS AND METHODS

Materials. All chemicals were of reagent-grade quality. They were purchased from commercial sources and used as received. The PAN polymer matrix used in this work is a copolymer containing 92% acrylonitrile and 8% vinyl acetate, supplied by Montefibre SpA. *N*,*N*-Dimethylformamide ≥99.8%, AnalaR NORMAPUR was purchased from VWR International PBI srl, Milano, Italy. Ultrapure water used for the coagulation bath and for the preparation of the analytical samples was produced by an RO system Purelab Option SR-7, Conductivity <2000 μS/cm (Elga Veolia, UK). $\{Ca^{II}Zn^{II}_6[(S,S)\text{-Mecysmox}]_3(OH)_2(H_2O)\}\cdot 12H_2O$ (1) was prepared following a previously reported procedure.[44,45]

MOF Synthesis. *Preparation of* $\{Ca^{II}Zn^{II}_6[(S,S)\text{-Methox}]_3(OH)_2(H_2O)\}\cdot 16H_2O$ *(**2**).* An aqueous solution (35 mL) of H_2Me_2-(*S*,*S*)-methionine (2.3 g, 6 mmol) and a 25% methanolic solution of Me_4NOH (7.35 mL, 18 mmol) were added dropwise to another aqueous solution containing $Zn(NO_3)_2\cdot 6H_2O$ (3.55 g, 12 mmol) and $CaCl_2$ (0.22 g, 2 mmol) in 20 mL. The resulting suspension was stirred overnight, and a white powder was obtained and collected by filtration and washed with water and methanol. Yield: 1.45 g, 44%. Anal.: calcd. for $C_{36}Zn_6CaH_{84}S_6N_6O_{37}$ (1817.88): C, 23.79; H, 4.66; N, 4.62; S, 10.58%. Found: C, 24.01; H, 4.51; N, 4.63; S, 10.51%.

https://doi.org/10.1021/acsami.4c12363
ACS Appl. Mater. Interfaces 2024, 16, 51182−51194

Alternatively, well-shaped hexagonal prisms of **2**, suitable for X-ray structural analysis, could be obtained by slow diffusion, in an H-shaped tube, of H_2O/DMF (1:1) solutions containing stoichiometric amounts of H_2Me_2-(*S*,*S*)-Methox (0.023 g, 0.06 mmol) and Me_4NOH (74 μL, 0.18 mmol) in one arm and $CaCl_2$ (0.0022 g, 0.02 mmol) and $Zn(NO_3)_2{\cdot}6H_2O$ (0.035 g, 0.12 mmol) in the other. They were isolated by filtration on paper and air-dried. Anal.: calcd. for $C_{36}Zn_6CaH_{84}S_6N_6O_{37}$ (1817.88): C, 23.79; H, 4.66; N, 4.62; S, 10.58%. Found: C, 23.69; H, 4.31; N, 4.61; S, 10.59%.

Preparation of $(CdCl_2)$*@{*$Ca^{II}Zn^{II}_6$*[(S,S)-Mecysmox]*$_3(OH)_2(H_2O)\}\cdot 8H_2O$ (**$CdCl_2$@1**) *and* $[Pb(NO_3)_2]_{0.5}$*@{*$Ca^{II}Zn^{II}_6$*[(S,S)-Mecysmox]*$_3(OH)_2(H_2O)\}\cdot 9H_2O$(**$[Pb(NO_3)_2]$@1**). Well-formed hexagonal green prisms of **$CdCl_2$@1** and **$[Pb(NO_3)_2]$@1**, which were suitable for X-ray diffraction, were obtained by soaking crystals of 1 (5.0 mg) in saturated H_2O/CH_3OH (1:1) solutions of **$CdCl_2$** and **$Pb(NO_3)_2$**, respectively, for 72 h. The crystals were washed with water, isolated by filtration on paper, and air-dried. **$CdCl_2$@1**: Anal.: calcd for $C_{30}Cl_2Zn_6CaCdH_{56}S_6N_6O_{29}$ (1772.76): C, 20.32; H, 3.18; S, 10.85; N, 4.74%. Found: C, 20.31; H, 3.11; S, 10.41; N, 4.53%. IR (KBr): ν = 1613 cm^{-1} (C═O). Anal.: calcd for $C_{30}Zn_6CaPb_{0.5}H_{58}S_6N_7O_{33}$ (1773.09): C, 20.32; H, 3.30; S, 10.85; N, 5.53%. Found: C, 20.21; H, 3.47; S, 10.59; N, 5.63%. IR (KBr): ν = 1609 cm^{-1} (C═O).

Physical Techniques. Elemental (C, H, N), TGA analyses and powder X-ray diffraction analyses (of the pure MOFs and of the MOFs used as fillers in the PAN matrix) were performed at the Microanalytical Service of the University of Calabria. ICP-MS analyses for the Pb^{2+}, Cd^{2+}, and Hg^{2+} and interferent ion capture experiments on the membrane (vide infra) were performed at the Department of Chemistry of the University of Calabria. FT−IR spectra were recorded on a PerkinElmer 882 spectrophotometer as KBr pellets. All characterizations confirmed the purity of the sample when compared with the previous work reported by us.[36,39]

Gas Adsorption. The N_2 adsorption−desorption isotherms at 77 K were carried out on polycrystalline samples of **1** and **2** with a BELSORP-mini-X instrument. Samples were first activated with methanol and then evacuated at 348 K for 16 h under 10^{-6} Torr prior to their analysis. The same procedure was repeated with the corresponding membranes.

X-ray Powder Diffraction Measurements. The experimental powder X-ray diffraction (PXRD) patterns of MOFs **1** and **2** were measured in order to confirm their structural stability. Thus, polycrystalline samples of **1** and **2** were introduced into 0.5 mm borosilicate capillaries prior to being mounted and aligned on a Bruker D2 Phaser powder diffractometer using Cu Kα radiation (λ = 1.54056 Å). Five repeated measurements were collected at room temperature (2θ = 2−50°) and merged in a single diffractogram.

On the other hand, the flexible disks of an average diameter of 34 ± 1 mm for both PAN and **BioMOF@PAN** membranes have been allocated on a plate sample holder and then mounted and aligned on a Bruker D2 Phaser powder diffractometer, using Cu Kα radiation (λ = 1.54056 Å). Three repeated measurements were collected at room temperature (2θ = 2−50°) and merged into a single diffractogram.

Scanning electron microscopy (SEM) analysis of the MOFs was carried out with an XL 30 ESEM (PHILIPS) microscope. Analysis of the membranes was carried out with a Phenom Pro X desktop SEM (Phenom-World, Eindhoven, NL), equipped with a backscattering detector. The images of the membrane morphology were acquired with an accelerating voltage of 10 kV. The samples were not sputter-coated with gold to avoid the backscattering signal of the MOF particles being covered by the stronger signal of the gold itself. As a result, the sample resolution and attainable magnification are somewhat lower due to charging of the sample.

X-ray Crystallographic Data Collection and Structure Refinement. Crystals of **2**, **$CdCl_2$@1**, and **$PbCl_2$@1**, with dimensions of ca. 0.08 × 0.08 × 0.10; 0.16 × 0.12 × 0.10, and 0.14 × 0.08 × 0.10 mm, respectively, were selected and mounted on a MITIGEN holder in Paratone oil. Measurements on single crystals of **$CdCl_2$@1** and **$[Pb(NO_3)_2]$@1** were performed at room temperature, whereas the single crystal of **2** was very quickly placed in a nitrogen stream cooled at 100 K to avoid possible degradation upon dehydration. Diffraction data were collected using synchrotron radiation at I19 beamlines in DIAMOND (λ = 0.6889 Å) for **2** or on a Bruker-Nonius X8APEXII CCD area detector diffractometer using graphite-monochromated Mo Kα radiation (λ = 0.71073 Å) for **$CdCl_2$@1** and **$[Pb(NO_3)_2]$@1**. The data were processed through xia2 software[46−50] (**2**) or processed through SAINT[51] reduction and SADABS[52] multiscan absorption software (**$CdCl_2$@1** and **$PbCl_2$@1**). The structures were solved with the SHELXS structure solution program, using the Patterson method. The model was refined with version 2018/3 of SHELXL against F^2 on all data by full-matrix least-squares.[52−54] Crystals of **$CdCl_2$@1** and **$[Pb(NO_3)_2]$@1**, suitable for X-ray diffraction, were obtained by soaking crystals of **1** (5.0 mg) in a saturated aqueous solution of $CdCl_2$ and $Pb(NO_3)_2$ for 10 days, after a crystal-to-crystal transformation. For these reasons, it is reasonable to observe a diffraction pattern sometimes affected by the expected internal imperfections of the crystals. All non-hydrogen atoms were refined anisotropically in **2** and **$CdCl_2$@1** except for some carbon and sulfur atoms belonging to the highly thermally disordered methionine and methylcysteine chains pointing within huge pores and disordered solvent water molecules or Cd and Pb atoms in **$CdCl_2$@1** and **$[Pb(NO_3)_2]$@1**, respectively. In the latter, due to the very low power of diffraction and in order to improve the reflections to parameters ratio, only the Zn^{2+} and Ca^{2+} were refined anisotropically. The occupancy factors of Cd^{2+} (0.333) and Pb^{2+} (0.1667) metal ions have been defined, in agreement with SEM results. Both Cd^{2+} and Pb^{2+} metal ions exhibit thermal disorder, as normally expected in porous crystals for captured molecules/ions. Indeed, the cadmium metal ions are detected residing at 2.64 Å from oxamate of the amino acid derivative and 3.99 Å from sulfur. On the contrary, the softer nature of Pb^{2+} ions brings them close to sulfur belonging to the methylcysteine derivative at a distance of 3.29 Å. In all crystal structure refinements, the use of some C−C and C−S bonds together with Pb−S bond, in **$[Pb(NO_3)_2]$@1**, length restraints during the refinements of some highly disordered atoms have been reasonably imposed and related to ethyl- and methyl-thiomethyl chains of the methox and mecysmox ligands, respectively, that are dynamic components of the frameworks. In the refinement of the crystal structure, some further restraints, to make the refinement more efficient, have been applied. For instance, ADP components have been restrained to be similar to other related atoms, using SIMU 0.02 for disordered sections or EADP for groups of atoms expected to have essentially similar ADPs. All the hydrogen atoms of the net were set in calculated positions and refined isotropically using the riding model. The large disordered sites for atoms belonging to the terminal chains residing in large pores imposed the need to fix their positions.

The solvent molecules in both models, together with NO_3^- and Cl^- anions expected in **$[Pb(NO_3)_2]$@1** and **$CdCl_2$@1**, were disordered, and no reasonable models have been found to define them. The hydrogen atoms of the ligand were set in calculated positions and refined as riding atoms, whereas water molecules were neither found nor calculated. A summary of the crystallographic data and structure refinement for **2**, **$CdCl_2$@1**, and **$[Pb(NO_3)_2]$@1** is given in Table S1. The comments for alerts A and B are reported in the CIFs using the validation response form (vrf). The somewhat high *R* values (levels Alert A and B in checkCIFs) are most likely affected by the contribution of the highly disordered solvent and anions to the intensities of the low angle reflections. CCDC (Cambridge Crystallographic Data Centre) reference numbers are 2354976, 2354977, and 2354978 for **2**, **$CdCl_2$@1**, and **$[Pb(NO_3)_2]$@1**, respectively. The final geometrical calculations on free voids and the graphical manipulations were carried out with PLATON,[55,56] implemented in WinGX,[55,56] and CRYSTAL MAKER[57] programs, respectively.

Membranes Preparation and Morphology Optimization. *Membrane Casting.* The neat PAN and MMM-MOFs were prepared by the nonsolvent-induced phase separation (NIPS) method. PAN was dissolved in DMF at 12 wt % under stirring at 60 °C until a clear and apparently homogeneous solution was obtained. For MMM-MOFs, BioMOFs **1** and **2**, as nanocrystalline powder, were added into the polymeric solution (50 wt % ratio polymer/MOF) and after mixing the mixture was sonicated for 1 h at 60 °C. The dispersion was

https://doi.org/10.1021/acsami.4c12363
ACS Appl. Mater. Interfaces 2024, 16, 51182−51194

then left standing for at least 30 min to remove air bubbles. The obtained solution or dispersion was cast by casting knife (Elcometer Instruments Inc., Manchester, England), with a gap of 450 μm, on a glass plate, and after 1 min, the film was immersed in the coagulation bath of pure water or water/solvent mixtures.

Membrane Characterization. The morphology of the neat PAN membrane was first optimized to obtain a sponge-like structure with fine uniform porosity, for guaranteeing a more consistent and intimate contact between the metal solution and the membrane, and for improving the interaction between the MOFs and the heavy metals to be captured. The composition of the coagulation bath was varied to tailor the membrane morphology. The addition of solvent in the coagulation bath delays the demixing process and therefore favors the formation of membranes with a spongy morphology. Neat PAN membranes were prepared with a range of different compositions of the coagulation bath, with a DMF/H_2O weight ratio ranging from 50/50 to 80/20 wt ratio, with intervals of 10% (Figure S4). The obtained membranes were stored in water until the absorption and flux measurements. The desired sponge-like morphology was obtained using a coagulation bath composition of 80/20 wt ratio DMF/H_2O. The optimized conditions were used for the MMMs' preparation. Figure 5 shows the morphology of the neat PAN membranes prepared by varying the coagulation bath composition. The finger-like morphology of the membrane gradually changes in a sponge-like morphology by increasing the solvent/nonsolvent ratio.

The addition of the BioMOFs **1** and **2** in the polymeric matrix is evidenced by the presence of small spherical particles homogeneously distributed inside the membrane having an average size lower than 1 μm and formed by smaller primary particles with an average diameter of ≈ca. 100 nm (Figure S5). The results of EDX analysis and mapping confirm the presence and the homogeneous distribution of the BioMOF filler in the polymer matrix. Specific elements of the BioMOFs, such as S, Zn, and Ca, are present in both membranes.

The highly porous structure of the membrane, firmly hosting the nanosized BioMOF particles (no leakage was observed at the end of the experiments), guarantees high permeability and a large surface area for the contact and successive adsorption of ions present in the solutions.

Tensile Tests. The mechanical properties of the membranes were studied by means of tensile tests, using a Zwick Roell single-column universal testing machine; model Z2.5 with a 100 N maximum load cell and pneumatic clamps with a rubber surface to increase friction with the sample. The membrane samples were fixed in the pneumatic clamps at an effective sample length of 3 cm and tested at a constant speed of 6 mm min^{-1} (corresponding to a deformation rate of 20% min^{-1}). For each membrane sample, at least 4−6 rectangular test strips of 5.0 mm width were tested, and the stress−strain curves were analyzed by the TestXpert III V1.161 software, calculating the average and standard deviation of Young's modulus, the tensile strength, and the maximum deformation at break.

Surface Roughness Measurement. Surface profile acquisition was performed using a Universal Optical Profilometer (Rtec UP-24, CH) in order to acquire the profile of the top surface of each membrane and to determine different profile roughness parameters, i.e., average roughness (R_a), root-mean-square roughness (R_q), and total height roughness (R_t). The sampling length was set as 8 mm.

Membranes Performance Tests. *Pure Water Permeability Tests.* Pure water permeability tests were carried out to determine the average residence time of the water phase as a function of applied pressure. The experiments were carried out with a Millipore UF Solvent Resistant Stirred Cell 47 mm XFUF04701, with an active area of 13.84 cm^2. The cell was pressurized with nitrogen, and the pressure was read with an analog manometer Spriano (Milano, Italy), model A49681 class 0.25 with a precision of 0.05 bar (Scheme S1). All measurements were carried out in the range of 1−5 bar, at 1 bar intervals. Measurements were repeated twice at each pressure. The weight of the permeate was measured as a function of time, taking 15 points for each pressure, using a Gibertini EU4000 AR electronic balance (4 decimal places) with ScaleCOM software for automatic registration of the permeate weight. A total of 0.5−2 g of water was collected for the neat PAN membrane, and 3−15 g for the MMMs.

No significant deviation from linearity was observed during single measurements of the flow rate as a function of the time. The neat PAN membrane showed a lower permeability than the BioMOF@PAN MMMs, and the permeability further decreased with increasing pressure, while the permeability of the MMMs was virtually pressure-independent. In the neat PAN membrane, a shrinking of the pores likely occurs as a result of the increased pressure, with a consequent decrease in water permeability. The presence of the BioMOFs probably confers additional structural stability to the membranes, which do not undergo mechanical deformations due to the increase in pressure.

Contact Time Optimization and Capture Experiments. The heavy metal sorption by MOFs is usually characterized by very fast kinetics. The water permeation rate must nevertheless be set low enough to guarantee an average contact time of the membrane with the permeating liquid of at least several seconds to ensure the maximum removal efficiency of heavy metals from the water matrix.

The average contact time, τ, of the fluid with the membrane is given by

$$\tau = l/v \tag{1}$$

where l is the membrane thickness (m) and v is the average linear velocity (m s^{-1}). The linear fluid velocity is given by the ratio of the measured flow rate J (m^3 s^{-1}) and membrane area A (m^2):

$$v = J/A \tag{2}$$

The average contact-time rapidly increases when decreasing the applied pressure and consequently the flow rate (Figure S7), showing an exponential dependence of the contact time as a function of pressure for all of the investigated membranes. High values of contact time were obtained with pressure <1 bar. Therefore, the absorption tests were carried out at the minimum feasible pressure (0.1 bar) to maximize the contact time.

We calculated the adsorption efficiency and the equilibrium loading as follows:

Removal efficiency (R%)

$$R_{i(\%)} = \left(1 - \frac{C_{P,i}}{C_{F,i}}\right) \times 100 \tag{3}$$

where $C_{F,i}$ and $C_{P,i}$ are the heavy metal concentrations in the feed and in the permeate, respectively.

$$Q_e = (C_0 - C_e)V/m \tag{4}$$

where C_0 and C_e are the initial and equilibrium concentrations (mg/L), respectively, V is the volume of the solution (L), and m is the mass of the adsorbent (g).

The absorption tests were carried out at the minimum feasible pressure (0.1 bar) to maximize the contact time. For the evaluation of the removal efficiency, a multielement solution containing Pb-$[(NO_3)]_2$, $CdCl_2$, and $HgCl_2$ and common interfering ions (such as Na^+, K^+, Ca^{2+}, Mg^{2+}, Cl^-, HCO_3^-, NO_3^-, and SO_4^{2-}), at room temperature, was used under dynamic conditions using the system reported in Scheme S1. The variation of the concentration of the heavy metals in the permeate was monitored through ICP-MS analysis on a number of samples collected over time (Tables S1−S5). All the samples were stabilized by adding 100 μL of nitric acid with a purity of 98%. Each experiment was performed in triplicate, and results are reported as average values of ±3SD.

RESULTS AND DISCUSSION

MOF Synthesis and Structures. BioMOFs **1** and **2** were prepared following an improved synthetic strategy, compared to that used for the previously reported isoreticular BioMOFs containing Cu(II) as metal ions,[36−42] which required the preparation and isolation of the corresponding $[Cu_2(L)]^{2-}$

https://doi.org/10.1021/acsami.4c12363
ACS Appl. Mater. Interfaces 2024, 16, 51182−51194

precursors. Zn-based MOFs **1**[44,45] and **2** are prepared following a more straightforward strategy consisting of the direct precipitation after mixing stoichiometric amounts of deprotonated ligands and Zn^{2+} and Ca^{2+} cations, which facilitates their large scale preparation.[36,39] In particular, the synthesis of **1** was reported very recently[44] in a previous work, whereas the synthesis and synchrotron crystal structure of **2** are here reported and described in detail in the Materials and Methods section.

The two chiral three-dimensional (3D) BioMOFs **1** and **2** were prepared using ligands derived from the natural amino acids *S*-methyl-L-cysteine and (S)-methionine, respectively. Both feature functional hexagonal channels decorated with thioether ($-(CH_2)_n-S-CH_3$) groups from the amino-acid residues, but with different pore sizes (Figure 1). The presence of thioether groups pointing toward the accessible void space of the BioMOFs (Figures 1 and S1), along with the high flexibility of the porous framework, offers a valuable microenvironment for interaction with metal ions. In particular, the softer Hg(II) ion displays a good binding tendency for sulfur coordination sites,[58] while the affinity is expected to gradually decrease for the Pb^{2+} and Cd^{2+} cations,[59,60] although examples exist reporting affinity interactions of Hg^{2+} toward cooperative oxygen sites.[61] Crystal structures of BioMOFs **1**[44] and **2** were determined by single crystal X-ray diffraction (Figure 1), and their bulk was fully characterized through thermogravimetric analysis (TGA), N_2 adsorption, and X-ray powder diffraction (Figures S2−S4). The morphology of polycrystalline samples of BioMOFs **1** and **2** determined by scanning electron microscopy (SEM) can be seen in Figures S5 and S6, respectively. Interestingly, both BioMOFs exhibit similar particle sizes in the range of 70−200 nm, which are in principle suitable for their incorporation in PAN MMM-MOFs.[62]

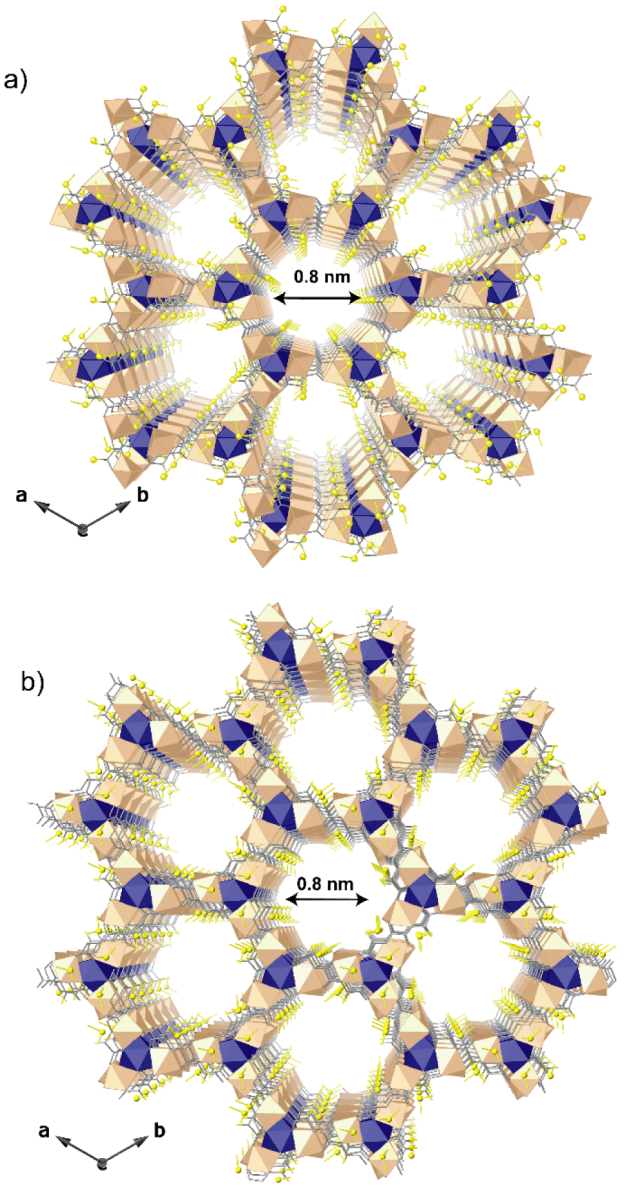

Figure 1. View of the porous crystal structures of **1** (a) and **2** (b) emphasizing their functional channels decorated with $-CH_2SCH_3$ and $-CH_2CH_2SCH_3$ groups for **1** and **2**, respectively. Zn and Ca are represented as orange and blue polyhedra, respectively. Organic ligands are depicted as gray sticks with the exception of sulfur atoms (yellow spheres).

The permanent porosity of BioMOFs **1** and **2**, was confirmed by their N_2 adsorption isotherms (Figure S3). The calculated Brunauer−Emmett−Teller (BET) surface areas were 682 and 455 m^2/g,[63] respectively, with calculated pores[64] of 0.74 nm (**1**) and 0.49 nm (**2**), similar to that observed in the crystal structure for **1** and reduced with respect to that found in the crystal structure of **2** (Figure 1).

This discrepancy is expected and likely due to the higher flexibility of thioether groups, confined in the pores of **2** that can be elongated after the activation process. The similarity in pore dimensions detected by SCXRD is only related to the snapshot of **2**, referring to bent thioether conformations.

In order to corroborate the possible pathways of interactions leading to Pb^{2+}, Cd^{2+}, and Hg^{2+} capture for the two BioMOFs, single crystal to single crystal loading experiments have been set. Systematic optimization of the crystallization conditions allowed us to obtain single crystals of **1** after absorption of metal ions from water, and thus, we determined the structures of the two hybrid materials $\mathbf{CdCl_2@1}$ and $\mathbf{[Pb(NO_3)_2]@1}$. These compounds were obtained by soaking single crystals of **1** in a water solution containing a suitable metal salt. In particular, 10 mg of **1** was soaked with 2 mL of a 2000 ppb solution of the corresponding metal salt for 10 days (replacing the aqueous solution every 24 h). EDX analysis performed on a sample of **1** after 10 days of soaking provided us with the following results: 6.5 and 5.9 wt % for $\mathbf{CdCl_2@1}$ and $\mathbf{[Pb(NO_3)_2]@1}$, respectively, which confirmed the presence of Cd(II) and Pb(II) in the framework structures. The maximum loading was 837 mg g^{-1} for lead and 923 mg g^{-1} for cadmium after 30 days of soaking.

No degradation of the crystals was observed, which completely retained their single-crystallinity, and the crystal structure of the hybrid materials $\mathbf{[Pb(NO_3)_2]@1}$ and $\mathbf{CdCl_2@1}$ could be resolved by single crystal X-ray diffraction (Figures 2 and S7).

The structures of $\mathbf{[Pb(NO_3)_2]@1}$ and $\mathbf{CdCl_2@1}$ are isoreticular to **1**. They crystallize in the chiral $P6_3$ space group of the hexagonal system (Table S1) and consist of honeycomb-like 3D Ca(II)−Zn(II) networks. The uninodal six-connected *acs* net is built up from trans-oxamidato-bridged zinc(II) units, $\{Zn^{II}_2[(S,S)\text{-Mecysmox}]\}$, which act as linkers between the Ca(II) ions through the carboxylate groups. In the resulting porous net, the functional $-CH_2SCH_3$ groups of the amino acid decorate the walls of the hexagonal channels with a

https://doi.org/10.1021/acsami.4c12363
ACS Appl. Mater. Interfaces 2024, 16, 51182−51194

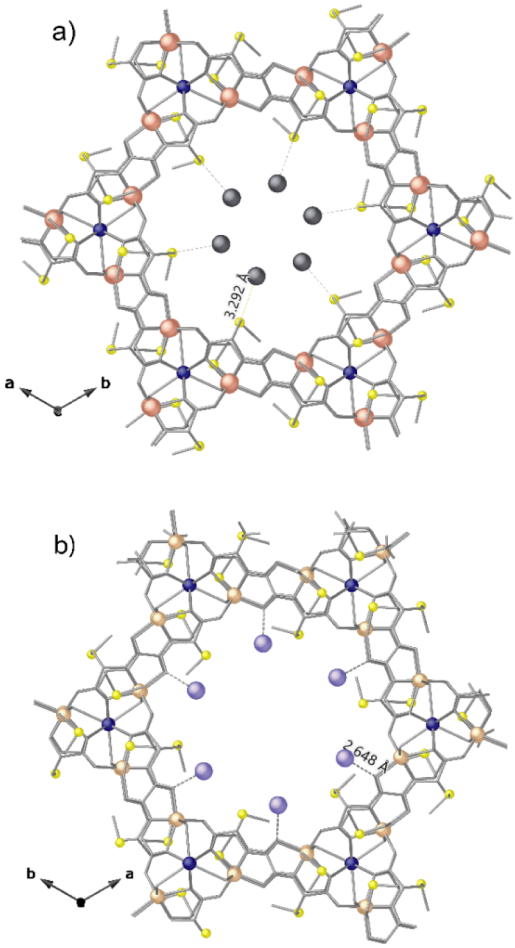

Figure 2. Perspective view of $[Pb(NO_3)_2]$**@1** (a) and $CdCl_2$**@1** (b) crystal structures along the *c* crystallographic axis. Color code: same as Figure 1.

diameter of ca. 0.8 nm. In the crystal structures of $[Pb(NO_3)_2]$**@1** and $CdCl_2$**@1**, the guest species reside in the hexagonal channels of the MOF, being anchored by interactions with the sulfur atoms from the thioether arms or the oxygen atoms of the oxamidato ligands decorating the pore walls, for Pb (II) and Cd(II), respectively, in perfect agreement with the Hard–Soft Acid–Base theory. These results definitely confirm that S···Pb [3.3 Å] and O···Cd [2.64 Å] interactions are at the origin of the material receptor properties for the selective metal capture process (Figures 2 and S7).

Evaluation of the Metal Adsorption Performance of 1 and 2. The removal efficiency and the equilibrium loading (Q_e) of **1** and **2**, defined as the amount of solute adsorbed per unit weight of solid at equilibrium, were first measured by soaking for 24 h a crystalline sample (50 mg) of each BioMOF in 100 mL of a 1 ppm aqueous solution containing either $Pb(NO_3)_2$, $CdCl_2$, or $HgCl_2$ metal salt. Small aliquots of samples were extracted after 72 h, and the metal ratio was monitored through ICP-AES. Results are shown in Figure 3. **1** showed the best performance for all the heavy metal cations, with removal efficiencies of 100, 82.1, and 100%, and Q_e of 2340, 1718, and 1822 $\mu g\ g^{-1}$ for lead, cadmium, and mercury, respectively. On the other hand, **2** showed good results for mercury removal, with an efficiency of 89%, and a Q_e of 1550 $\mu g\ g^{-1}$, but its performance declined for lead and cadmium. In particular, **1** showed superior ability for Cd^{2+} capture, when

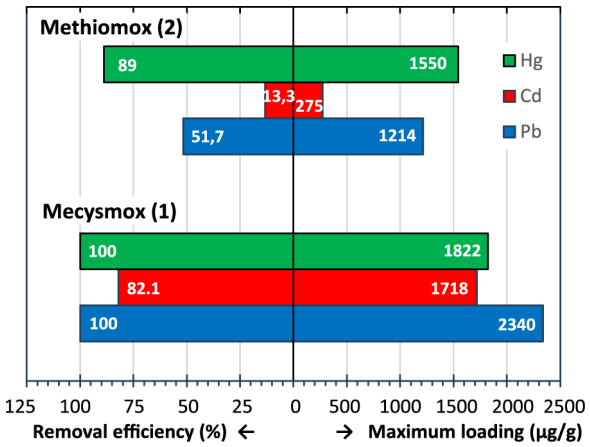

Figure 3. Equilibrium loading and removal efficiency after 72 h, determined by soaking 50 mg of polycrystalline samples of **1** and **2** in 100 mL of a 1 ppm aqueous solution containing the suitable metal salt.

considering the lower Q_e and removal efficiency recorded for **2** (275 $\mu g\ g^{-1}$ and 13.4%) under the same conditions. The Q_e and removal efficiency for lead ions are also substantially higher in **1** with respect to **2** (1214 $\mu g\ g^{-1}$ and 51.7%).

These results clearly situate **1** as the best adsorbent for all of the metal ions. Its superior performance can be attributed to the optimal combination of pore functionality and pore size, determined by the thioether arms[37−43,65,66] of the methyl cysteine residues in **1**.

The capture efficiency of the BioMOFs in more diluted multicomponent solutions was also evaluated by soaking polycrystalline powders of **1** and **2** (40 mg) for 60 min in 200 mL of a 300 ppb aqueous solution containing $Pb(NO_3)_2$, $CdCl_2$, or $HgCl_2$, dissolved in oligomineral water. Small aliquots of the solutions were extracted at different time intervals, and the metal ratio was monitored through ICP-AES. The trends are shown in Figure 4, and the numerical values are reported in Tables S2 and S3.

1 showed the best performance for the adsorption of all heavy metal cations, with very fast kinetics and a removal efficiency of 100, 45, and 92% for lead, cadmium, and mercury, respectively. The capture performance of **2** was modest

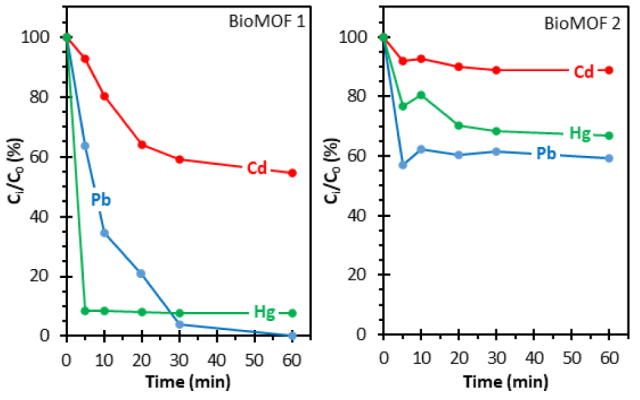

Figure 4. Relative concentration (C_i/C_0%) as a function of time for lead, cadmium, and mercury metal ions measured in static conditions for **1** (left) and **2** (right) (40 mg of polycrystalline samples of **1** and **2** in 200 mL of an aqueous solution containing 300 ppb of each metal salt).

https://doi.org/10.1021/acsami.4c12363
ACS Appl. Mater. Interfaces 2024, 16, 51182−51194

compared to **1**, with a removal efficiency of 40% for lead, 11% for cadmium, and 33% for mercury. This confirms **1** as the best adsorbent for all metal ions, even at lower concentrations.

Membrane Preparation, Morphology, and Properties. Based on the removal properties of **1** and **2** and aiming at obtaining more manageable and efficient materials, both MOFs were embedded in porous mixed matrix membranes. In a previous work,[37] we used Matrimid membranes, but their tendency to form macrovoids and finger-like void structures led to inefficient absorption. Therefore, in the present work, we used polyacrylonitrile (PAN), one of the most commonly used polymers for the fabrication of microfiltration membranes,[62] with a semicrystalline structure, in contrast to the amorphous Matrimid. Under optimum conditions, PAN may undergo solid−liquid demixing during the nonsolvent-induced phase inversion process or it may undergo liquid−liquid demixing followed by rapid crystallization, and this can be exploited to tailor the membrane morphology. PAN contains a nitrile group (−C≡N) in the polymer repeating unit, which mainly determines its hydrophilic properties.[62] It has high mechanical strength and fair thermal and chemical stability. It is resistant to acids and alkalis in a fairly wide pH range (from 2 to 12) and presents good chemical resistance to aliphatic hydrocarbons and alcohols.[67] The polymer also exhibits biocompatibility and sterilization resistance. Moreover, it is cheaper than the SWCNTs and Matrimid 5218 that we previously used as support materials.[37,66]

Porous films were prepared by nonsolvent-induced phase separation (NIPS). This is the only technique capable of producing the required highly porous tortuous morphology where the BioMOFs, chemically functionalized for selective and efficient adsorption, remain partially immobilized and trapped yet fully accessible for the surrounding liquid phase. For membrane preparation via phase inversion, PAN was dissolved in the aprotic polar solvent dimethylformamide (DMF).[68] Extensive optimization of the membrane formation process (polymer concentration, coagulation bath composition, and additives) was required to yield the desired sponge-like porous structure (Figure S8). A sponge-like morphology with a fine uniform porosity is also required to guarantee a more intimate contact between the metal solution and the membrane, and to improve the interaction between the MOFs and the heavy metals to be captured. Polyvinylpyrrolidone (PVP) is soluble in water and in the PAN solution, increasing its viscosity and slowing down the phase inversion process. Addition of PVP to the casting solution as a pore-former[69,70] helped to reduce the formation of macrovoids but was insufficient to yield a fully sponge-like morphology (Figure S8). Unfortunately, it was later found that PVP favors leaching of the MOF into the coagulation bath when making MMMs. As an alternative approach, addition of the DMF to the water coagulation bath to slow down the coagulation process[71,72] successfully yielded the required sponge-like morphology at 80% DMF in the water bath, even without the pore-former PVP (Figure 5).

The BioMOF@PAN MMMs, containing **1** and **2** (**1@PAN** and **2@PAN**), were prepared under the following optimized conditions: 15 wt % PAN in the casting solution and 80 wt % DMF in the coagulation bath (see Materials and Methods section for synthetic details). The highest possible amount of MOF that kept the solution sufficiently fluid for the casting of a homogeneous film was 15 wt %, corresponding to 50 wt % of the projected total MMM solid content, and was used for the

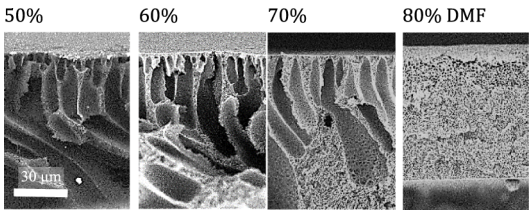

Figure 5. Cross-sectional images of neat PAN membranes prepared with increasing DMF fractions in the water coagulation bath. SEM magnification: 2500× ; acceleration voltage 10 kV. The scale bar is identical for all figures.

preparation of the membranes with both **1** and **2**. This is a relatively high MOF loading compared with other MMMs reported in the literature, which are usually dominated by polymer performance and low MOF loading (<50%).[73] Neat PAN membranes were used for comparison in all experiments since PAN contains −C≡N groups, which can also interact with the metal ions. The resulting membranes are extremely pliable and can deform to some extent when stretched. The morphology and microscopic texture of PAN and BioMOF@PAN membranes were characterized by scanning electron microscopy. Figure 6 shows the cross-sectional SEM images of

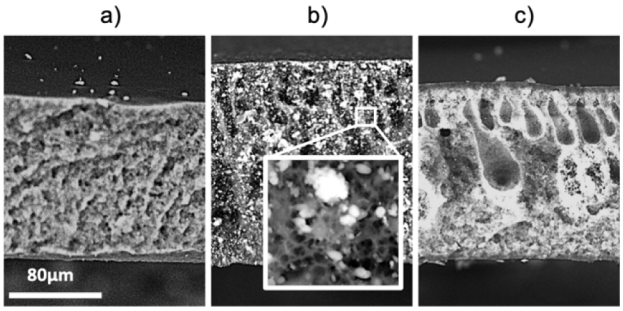

Figure 6. Representative cross-sectional SEM images (1000×, 15 kV) of neat PAN (a), **1@PAN** (b), and **2@PAN** (c). The brighter spots are the larger MOF clusters, highlighted by the backscattering detector, and confirm the uniform particle distribution. The scale bar is identical for all figures.

neat PAN and BioMOF@PAN membranes obtained under the above-mentioned conditions. A zoomed-in view of membrane **1@PAN** highlights the particles of **1** embedded in the PAN matrix. The surface and bottom images are shown in Figure S9.

The circular membranes all have an active average diameter of 47 ± 0.1 mm and an average thickness of 198 ± 13.2 μm for the neat PAN, while it was 185.4 ± 3.65 and 201.2 ± 2.95 μm for **1@PAN** and **2@PAN**, respectively. The average mass of the disks is 41.4 ± 2 mg for the PAN membrane and 35.9 ± 3 mg for both mixed matrix membranes, with a resulting density of 0.12 g cm^{-3} for neat PAN and 0.11 and 0.10 g cm^{-3} for **1@PAN** and **2@PAN**, respectively, confirming their high porosity.

All membranes are characterized by a smooth surface (Figure S9) and a spongy morphology. The presence of the BioMOFs in the membranes is evidenced by PXRD patterns (Figure S4c) where only a slight decrease of peak intensity compared to the MOFs is observed, as expected. The small MOF crystals with an average size of 1 μm are homogeneously dispersed in the polymer matrix (Figure S9). The highly microporous and stable structure of PAN firmly hosts the nanosized BioMOF particles, and no leakage of the MOF fillers was observed during the adsorption tests.

https://doi.org/10.1021/acsami.4c12363
ACS Appl. Mater. Interfaces 2024, 16, 51182−51194

The stability of the membrane is guaranteed by the fact that the size of the pore windows of the PAN membrane is smaller than the size of the dispersed BioMOF particles. As a result, the PAN matrix is formed around the BioMOF, and the BioMOF particles are free to move within the internal voids of the membrane (inset in Figure 6b), but they are trapped and cannot leave these voids.

Profile scans of the top surface of the membranes (Figures S11 and S12) were made to determine the average roughness (R_a), the root-mean-square roughness (R_q), and the total height roughness (R_t) of the membrane skin (Figure S10). The values of R_a and R_q all fall roughly in the range of 1−2 μm, indicating a relatively smooth surface of the membranes, considering their total thickness near 200 μm. The larger negative fluctuations of the profile in Figure S11 most likely represent larger voids just below the surface because the pores in the skin are submicrometer sized. The large and mostly overlapping error margins in Figure S11 do not allow any statistically relevant quantitative comparison of the membranes. The 10× higher values of R_t compared to R_a and R_q reflect the somewhat larger long-distance fluctuations in the membrane (Figure S12), most likely formed during the weak contraction of the polymer in contact with the nonsolvent.

The neat PAN membrane has a water permeability of 25 L m^{-2} h^{-1} bar^{-1} at 1 bar, which decreases to 16 L m^{-2} h^{-1} bar^{-1} when increasing the pressure to 5 bar, probably caused by the compression of the porous membrane structure (Figure 7).

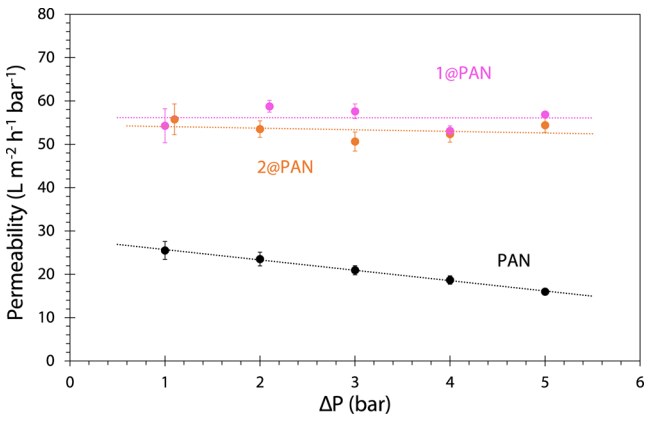

Figure 7. Permeability as a function of the applied pressure for the neat PAN and the **1@PAN** and **2@PAN** MMMs. The data indicate the average and standard deviation of 15 individual measurements.

The water permeability improves more than 2-fold to ca. 55 L m^{-2} h^{-1} bar^{-1} upon incorporation of the BioMOFs, as a result of the higher porosity or more open pore-structure (Figure 6) of the membranes. The high permeability is maintained with increasing pressure, suggesting that the BioMOFs also increase the mechanical stability of the overall membrane structure (Figure 7). Although the flat sheet membranes are subject to compression forces, tensile tests provide useful information about their general mechanical properties in relation to their composition and morphology. Tensile tests on a representative set of neat PAN membranes (row 1 with 3% PVP in Figure S8) show a rapid increase in Young's modulus and tensile strength at higher DMF concentrations in the nonsolvent bath (Figure S13), confirming the importance of the sponge-like morphology also from the mechanical point of view, besides that of providing optimum fluid dynamics. Tensile tests of the **1@PAN** and **2@PAN** membranes show good mechanical resistance, with an elastic modulus of 145 and 125 MPa, respectively, and a tensile strength of 4.1 and 3.3 MPa (Figure S13). These results show that the MMMs can withstand much higher stresses than the pressures applied during the permeation tests (<0.5 MPa), without the risk of rupture. The tensile strength becomes even more relevant in the case of hollow fiber membranes, for which the internal pressure translates into a transversal (tensile) force on the membrane wall.[70]

Evaluation of the Metal Adsorption Performance of Membranes. Most of the current technologies for heavy metal ion removal target a specific metal ion. Since water is often simultaneously polluted by a variety of heavy metal ions, a material that can simultaneously adsorb more than one species can be useful for practical application. Issues related to competitive adsorption due to different binding affinities toward active functional groups can lead to preferential adsorption for certain species, with respect to others. Lead, cadmium, and mercury are among the most common heavy metals that cause severe human poisoning. To evaluate the adsorption of multiple heavy metal ions, we conducted a screening process under dynamic conditions (refer to Supporting Information and Scheme S1). We employed an oligo-mineral aqueous solution (80 mL) containing the three metal ions, with initial concentrations of approximately 600 ppb for Hg(II) and 300 ppb for Pb(II) and Cd(II), along with various multiions as potential interferents. Given the good performance of **1** in mercury removal, the mercury solution was prepared at twice the concentration of those for cadmium and lead. Compared to our earlier work,[37] apart from the improved tortuous flow path through the sponge-like morphology present in the PAN-based membranes, the mass transfer and heavy metal removal efficiency were also improved by tailoring the contact time (see Materials and Methods section for synthetic details). Hence, the contaminated solution was filtered through both the pristine PAN membranes and the MMMs under low pressure. This approach aimed to decrease the flow rate and extend the contact time (>100 s) between the membrane bulk and the multicomponent solution, thereby enhancing the adsorption process (Figure S14). The heavy metal concentration in the permeate was monitored via periodic ICP-MS analysis to track the adsorption as a function of time (Tables S4−S6). To quantify the absorption of metal ions by the setup, a solution containing all metal salts was also analyzed under identical conditions and over the same time interval but without a membrane. The absence of a significant drop in metal concentrations during this test confirmed that there was no considerable adsorption by the experimental setup.

The amount of metal ions removed by BioMOF@PAN membranes was generally much higher than the amount adsorbed by the neat PAN membrane under the same conditions, as reported in Figures 8, S15, and S16 and Tables S4−S6, confirming the fundamental role of the MOFs within the membranes. Despite the presence of other ions in oligo-mineral water at much higher concentrations compared to the heavy metal pollutants, the composite material effectively removed the three heavy metal ions. This demonstrates the selective recognition and removal capabilities of the composite materials for heavy metal ions from water. Remarkably, considering the performance exhibited by the BioMOFs when utilized as polycrystalline powders, the removal efficiency

https://doi.org/10.1021/acsami.4c12363
ACS Appl. Mater. Interfaces 2024, 16, 51182−51194

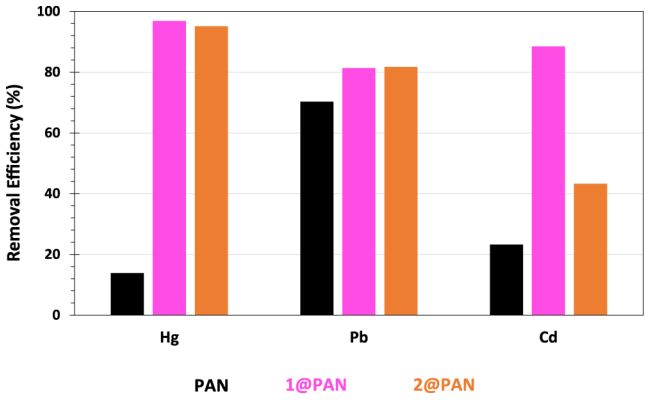

Figure 8. Removal efficiency for Pb^{2+}, Cd^{2+}, and Hg^{2+} for the neat PAN membranes and the MMMs containing **1** and **2**, after 12 h.

of each BioMOF embedded in the PAN matrix remains unchanged or even improves when filtering multiple ions simultaneously.

The neat PAN membrane removed lead with an efficiency of 70%, substantially better than those of Cd(II) (23.2%) and Hg(II) (13.9%). This must be attributed to a high affinity of the PAN polymeric matrix for lead, most likely in combination with a higher diffusion ability of Pb(II) ions within the pores of the membrane.[74] The significant increase in water permeability upon inclusion of BioMOF **1** and **2** in the PAN membrane (Figure 7) was accompanied by an enhancement in the absorption ability of the MMMs. The removal efficiency, R_i, is defined as the fraction of the heavy metals retained by the membranes (Figures 8 and S10), either through adsorption, or rejection, or both (eq 3).

A moderate increase was observed for lead ion capture compared to the PAN membrane (R = 81.3 and 81.7% for **1** and **2**, respectively). Additionally, a major improvement of the absorption ability for Cd^{2+} and, particularly, for Hg^{2+} (R = 23.2 and 13.9% for PAN, 88 and 96.8% for **1@PAN**, and 43.3 and 95.1% for **2@PAN**, for Cd^{2+} and Hg^{2+}, respectively) was achieved. The excellent capture capability of **1@PAN** and **2@PAN** membranes for cadmium, lead, and mercury ions, sometimes surpasses the performance of **1** and **2** in their powder form; the capture capability of the BioMOFs is not compromised by their inclusion of the polycrystalline powders in the PAN matrix; in fact, it appears to facilitate the transport and concentration of metal ions in proximity to the BioMOFs' surface.

Furthermore, the uptake of multiple metal ions in the pores of the BioMOFs does not appear to affect their performance, in terms of removal efficiency for each metal ion. This is attributed to the functional microenvironment provided by the porosity of the BioMOFs. It is conceivable that the adsorption of a specific metal ion within the BioMOFs' cavities can induce a favorable reorganization of the flexible functional groups decorating the BioMOFs' walls. This may enhance the microporous environment's receptivity toward the adsorption of additional different species. Indeed, it can be inferred—from the comparison of the structures of **[Pb(NO$_3$)$_2$]@1** and the previously reported one[37] from a host–guest aggregate formed by a Cu_6Ca isoreticular MOF with $HgCl_2$ molecules embedded (**$HgCl_2$@1**)—that competitive adsorption can mainly occur for mercury and lead metal ions in **1@PAN** and **2@PAN** membranes, since both Hg^{2+} and Pb^{2+} compete for coordination to the sulfur atoms of the amino acid residue, when entrapped within the BioMOFs' pores. Conversely, the snapshots provided by single-crystal X-ray structural determination of **$CdCl_2$@1** (also compared with **$HgCl_2$@1**[37] structure) suggest that Cd^{2+} and Hg^{2+} metal ions are principally recognized and trapped within the BioMOFs by means of two different structural functionalities. While S···Hg interactions involving the thioether groups are responsible for facilitating mercury capture, O···Cd interactions involving the oxamate moieties of the 3D framework primarily drive the capture of cadmium ions. Moreover, the thioether groups of the amino acid residue exhibit extreme flexibility, being able to assume a distended conformation inward the pores upon mercury coordination while forcing the other chains to adopt a strongly bent conformation.[37] This rearrangement can make the oxygen atoms of the BioMOF walls more exposed and accessible for cadmium binding. These changes are expected to occur more easily in **1** than in **2**, due to the presence of shorter thioether functional chains, which guarantee the optimal

Table 1. Comparison of Removal Efficiency (R%) for Some MOF-Based Adsorbent Materials

MOF-based adsorbent	Experimental conditions	Pb(II) initial concentration (mg/L)	Cd(II) initial concentration (mg/L)	Hg(II) initial concentration (mg/L)	Pb(II)R%	Cd(II) R%	Hg(II)R%	Ref.
			MOF microcrystalline powder					
Amino-functionalized ZIF-8	Batch experiment1 hMultielement aqueous solution	50	50	-	79.9	91.5	-	63
Methox/SeriMTV-MOF	Batch experiment48 hMultielement aqueous solutionBatch experiment72 hOligomineral waterBatch experiment24 hOligomineral water	1	-	1	99.4	-	99.5	43
Methox/MecysMTV-MOF		1	-	-	99.5	-	-	54
$CaCu_6$Mecys		-	-	10	-	-	100	37
$CaZn_6$Mecys	Batch experiment72 h (1 h) Oligomineral water	1 (0.3)	1 (0.3)	1 (0.3)	100 (100)	82 (45)	100 (92)	This work
			MOF-based composite materials					
MOF-808 CMC Aerogel	Batch experiment24 hAqueous solution	100	-	-	90	-	-	64
Methox/Mecys MTV-MOF/SWCNT-BP	Batch experiment72 hOligomineral water	0.31	-	-	100100	-	-	54
$CaCu_6$Mecys@ Matrimid	Filtration by recirculation48 hOligomineral water	-	-	0.3	-	-	99.6	37
1@PAN	Single pass filtration12 hMultielement solution	0.3	0.3	0.6	81.3	88.0	96.8	This work

https://doi.org/10.1021/acsami.4c12363
ACS Appl. Mater. Interfaces 2024, 16, 51182–51194

combination of recognition sites, pore size, and a more adaptive environment for metal ion sequestration.

Overall, these results, in comparison with previous reports,[37,43,66,75,76] (Table 1), clearly identify the BioMOF@PAN **1** membrane as a potentially effective material for capturing multiple heavy metal ions simultaneously from water. This makes it useful for the reduction of the concentration of these harmful species in drinking water in order to comply with regulatory contaminant limitations and meet the criteria for an efficient water reuse strategy.

Finally, since the stability during the potential regeneration of the membranes is a key factor for their successful industrial application, the performance of the **1@PAN** membrane during the regeneration process was also evaluated. Two of the main risks that could potentially compromise the successful industrial application of these novel membranes are the leaching of the MOF from the polymer matrix, as observed in our preliminary experiments under different coagulation conditions and the loss of sorption capacity due to pore blocking of the MOF or irreversible adsorption of trace contaminants. Therefore, the stability and the possibility to recycle the **1@PAN** membrane were evaluated by repeating the sorption experiments three times, alternating the tests with a regeneration step by washing the membranes with 250 mL of ethanol. It was found that the membrane showed nearly complete efficiency recovery after each regeneration process, losing less than 1% of the original adsorption capacity.

Further optimization of the membrane morphology to produce tight nanofiltration membranes, where part of the separation takes place by size exclusion or Donnan exclusion[77] and where only a fraction of the heavy metals needs to be adsorbed in the MOFs or in the membrane bulk, offers important future perspectives for a further enhancement of their separation performance and for a reduction of the regeneration frequency.

CONCLUSIONS

In this study, PAN membranes loaded with high concentrations of different BioMOFs were successfully prepared via the NIPS method. The presence of the BioMOFs, in particular those containing the *S*-methyl-L-cysteine amino acid residues (**1**), assured highly efficient heavy metal ion adsorption from oligomineral water. The improved adsorption performance for the simultaneous removal of all the metal ions observed for BioMOF@PAN membranes can be attributed mostly to the functional microenvironment of the BioMOFs, which provide convenient recognition sites for metal sequestration. Additionally, in the case of Pb^{2+}, this improvement can also be attributed to a significant affinity of the metal ion for the polyacrylonitrile itself. The thioether groups of the amino acid residues in **1** and **2** establish preferential interactions with the softer Hg^{2+} and, to a minor extent, with Pb^{2+} cations through the sulfur atom, while the Cd^{2+} cation is preferentially recognized by the oxygen atoms of the oxamate ligands. The BioMOF@PAN membranes containing **1** displayed the best performance, most likely due to a combination of the opportune pore size and porosity for metal capture. Indeed, while **1** contains short-chain thioether functionality from the cysteine-derived bioligand, **2** contains methionine-derived ligands with longer thioether functional groups, which reduce the pore size and increase the steric hindrance within the channels (see the BET values). Optimizing the membrane preparation conditions to tailor the morphology, increase the tortuosity, and enhance the MOF loading, along with a careful selection of the operation conditions to maximize the contact time of the solution with the membrane, enables highly efficient heavy metal removal in a single pass. Furthermore, successful regeneration by simple alcohol purging to remove the absorbed metals makes these membranes promising candidates for practical application in water remediation.

ASSOCIATED CONTENT

Supporting Information

2 The Supporting Information is available free of charge at https://pubs.acs.org/doi/10.1021/acsami.4c12363.

Crystallographic data for **2**, $[\mathbf{Pb(NO_3)_2}]$**@1**, and $\mathbf{CdCl_2}$**@1** (Table S1); residual Pb^{2+}, Cd^{2+}, and Hg^{2+} concentrations (Tables S2−S6); set-up for the water permeability measurements (Scheme S1); perspective view (Figures S1 and S7); thermogravimetric analysis (Figure S2); N_2 adsorption isotherms of **1** and **2** (Figure S3); calculated and experimental PXRD patterns profiles (Figure S4); SEM images (Figures S5, S6, S8, and S9); roughness parameters (Figure S10); roughness profiles (Figure S11); screen of scanned surfaces (Figures S12); (a) Young's modulus, (b) ultimate tensile strength, and (c) elongation at break (Figure S13); contact time as function of the pressure (Figure S14); removal efficiency upon time (Figures S15 and S16) (PDF)

Crystal structure of **2** (CIF)

Crystal structure of $[\mathbf{Pb(NO_3)_2}]$**@1** (CIF)

Crystal structure of $\mathbf{CdCl_2}$**@1** (CIF)

Accession Codes

CCDC 2354976−2354978 contain the supplementary crystallographic data for this paper. These data can be obtained free of charge via www.ccdc.cam.ac.uk/data_request/cif, or by emailing data_request@ccdc.cam.ac.uk, or by contacting The Cambridge Crystallographic Data Centre, 12 Union Road, Cambridge CB2 1EZ, UK; fax: + 44 1223 336 033.

AUTHOR INFORMATION

Corresponding Authors

Teresa F. Mastropietro − *Dipartimento di Chimica e Tecnologie Chimiche, Università della Calabria, Rende, Cosenza 87036, Italy*; Email: teresafina.mastropietro@unical.it

Johannes C. Jansen − *Institute on Membrane Technology, CNR-ITM, Rende, Cosenza 87036, Italy*; orcid.org/0000-0003-4538-6851; Email: johannescarolus.jansen@cnr.it

Emilio Pardo − *Instituto de Ciencia Molecular (ICMol), Universidad de Valencia, Paterna, Valencia 46980, Spain*; orcid.org/0000-0002-1394-2553; Email: emilio.pardo@uv.es

Donatella Armentano − *Dipartimento di Chimica e Tecnologie Chimiche, Università della Calabria, Rende, Cosenza 87036, Italy*; orcid.org/0000-0002-8502-8074; Email: donatella.armentano@unical.it

Authors

Paula Escamilla − *Instituto de Ciencia Molecular (ICMol), Universidad de Valencia, Paterna, Valencia 46980, Spain*

Marcello Monteleone − *Institute on Membrane Technology, CNR-ITM, Rende, Cosenza 87036, Italy*

Rita Maria Percoco − *Dipartimento di Chimica e Tecnologie Chimiche, Università della Calabria, Rende, Cosenza 87036, Italy*
Mariagiulia Longo − *Institute on Membrane Technology, CNR-ITM, Rende, Cosenza 87036, Italy*
Elisa Esposito − *Institute on Membrane Technology, CNR-ITM, Rende, Cosenza 87036, Italy*
Alessio Fuoco − *Institute on Membrane Technology, CNR-ITM, Rende, Cosenza 87036, Italy*; orcid.org/0000-0002-8355-0141
Rosangela Elliani − *Dipartimento di Chimica e Tecnologie Chimiche, Università della Calabria, Rende, Cosenza 87036, Italy*
Antonio Tagarelli − *Dipartimento di Chimica e Tecnologie Chimiche, Università della Calabria, Rende, Cosenza 87036, Italy*
Jesus Ferrando-Soria − *Instituto de Ciencia Molecular (ICMol), Universidad de Valencia, Paterna, Valencia 46980, Spain*
Valeria Amendola − *Dipartimento di Chimica Generale, Università di Pavia, Pavia 27100, Italy*; orcid.org/0000-0001-5219-6074

Complete contact information is available at: https://pubs.acs.org/10.1021/acsami.4c12363

Author Contributions

#P.E. and M.M. contributed equally. The manuscript was written through contributions of all authors. All authors have given approval to the final version of the manuscript.

Notes

The authors declare no competing financial interest.

■ ACKNOWLEDGMENTS

This work was supported by the Ministero dell'Università e della Ricerca (Italy), the MICINN (Spain) (Projects PID2022-136349OB-I00 and Excellence Unit "Maria de Maeztu" CEX2019-000919-M), and the Generalitat Valenciana (Project PROMETEO/2021/054). The authors also acknowledge the financial support of the Fondazione CARIPLO/"Economia Circolare: ricerca per un futuro sostenibile" 2019, Project code: 2019-2090, MOCA. Thanks are also extended to the "Ramon y Cajal Programme (RYC2019-027940-I)" (J.F.-S.). E.P. acknowledges the financial support of the European Research Council under the European Union's Horizon 2020 research and innovation programme/ERC Grant Agreement No. 814804, MOF-reactors. This study forms part of the Advanced Materials programme (MFA/2022/048) and was supported by MCIN with funding from European Union NextGenerationEU (PRTR-C17.I1) and by Generalitat Valenciana. D.A. acknowledges the financial support from European Union Next Generation EU (CUP C28H23000290002 − Project "NAIADI"). The authors acknowledge Prof. Carmine Maletta and Dr Pietro Magarò from the Dipartimento di Ingegneria Meccanica, Energetica e Gestionale, Università della Calabria, for their generous help in the acquisition of membrane surface profiles.

■ ABBREVIATIONS

CCR2, CC chemokine receptor 2; CCL2, CC chemokine ligand 2; CCR5, CC chemokine receptor 5; TLC, thin layer chromatography

■ REFERENCES

(1) Xu, L. *Impact of Climate Change and Human Activity on the Eco-Environment*; Springer: Berlin, Heidelberg, 2015.
(2) Sousa, J. C. G.; Ribeiro, A. R.; Barbosa, M. O.; Ribeiro, C.; Tiritan, M. E.; Pereira, M. F. R.; Silva, A. M. T. Monitoring of the 17 EU Watch List Contaminants of Emerging Concern in the Ave and the Sousa Rivers. *Sci. Total Environ.* **2019**, *649*, 1083−1095.
(3) Sousa, J. C. G.; Ribeiro, A. R.; Barbosa, M. O.; Pereira, M. F. R.; Silva, A. M. T. A Review on Environmental Monitoring of Water Organic Pollutants Identified by EU Guidelines. *J. Hazard. Mater.* **2018**, *344*, 146−162.
(4) Gavrilescu, M.; Demnerová, K.; Aamand, J.; Agathos, S.; Fava, F. Emerging Pollutants in the Environment: Present and Future Challenges in Biomonitoring, Ecological Risks and Bioremediation. *N. Biotechnol.* **2015**, *32*, 147−156.
(5) Schwarzenbach, R. P.; Escher, B. I.; Fenner, K.; Hofstetter, T. B.; Johnson, C. A.; von Gunten, U.; Wehrli, B. The Challenge of Micropollutants in Aquatic Systems. *Science* **2006**, *313*, 1072−1077.
(6) Deblonde, T.; Cossu-Leguille, C.; Hartemann, P. Emerging Pollutants in Wastewater: A Review of the Literature. *Int. J. Hyg. Environ. Health* **2011**, *214*, 442−448.
(7) EUR-Lex *Directive 2000/60/EC of the European Parliament and of the Council of 23 October 2000 establishing a framework for Community action in the field of water policy*; EUR-Lex.
(8) THE EUROPEAN COMMISSION *Commission Implementing Decision (EU) 2015/495 of 20 March 2015 establishing a watch list of substances for Union-wide monitoring in the field of water policy pursuant to Directive 2008/105/EC of the European Parliament and of the Council (notified under document C(2015) 1756)*. http://data.europa.eu/eli/dec_impl/2015/495/oj.
(9) Liu, X.; Wu, J.; Shi, W.; Shi, W.; Liu, H.; Wu, X. Lead Induces Genotoxicity via Oxidative Stress and Promoter Methylation of DNA Repair Genes in Human Lymphoblastoid TK6 Cells. *Med. Sci. Monit.* **2018**, *24*, 4295−4304.
(10) Genchi, G.; Sinicropi, M. S.; Lauria, G.; Carocci, A.; Catalano, A. The Effects of Cadmium Toxicity. *Int. J. Environ. Res. Public Health* **2020**, *17*, 3782.
(11) Ha, E.; Basu, N.; Bose-O'Reilly, S.; Dórea, J. G.; McSorley, E.; Sakamoto, M.; Chan, H. M. Current Progress on Understanding the Impact of Mercury on Human Health. *Environ. Res.* **2017**, *152*, 419−433.
(12) European Union *Regulation (EC) No 1907/2006 of the European Parliament and of the Council of 18 December 2006 concerning the Registration, Evaluation, Authorisation and Restriction of Chemicals (REACH), establishing a European Chemicals Agency, amending Directive 1999/45/EC and repealing Council Regulation (EEC) No 793/93 and Commission Regulation (EC) No 1488/94 as well as Council Directive 76/769/EEC and Commission Directives 91/155/EEC, 93/67/EEC, 93/105/EC and 2000/21/EC*; European Union.
(13) Ribeiro, A. R.; Nunes, O. C.; Pereira, M. F. R.; Silva, A. M. T. An Overview on the Advanced Oxidation Processes Applied for the Treatment of Water Pollutants Defined in the Recently Launched Directive 2013/39/EU. *Environ. Int.* **2015**, *75*, 33−51.
(14) Foteinis, S.; Borthwick, A. G. L.; Frontistis, Z.; Mantzavinos, D.; Chatzisymeon, E. Environmental Sustainability of Light-Driven Processes for Wastewater Treatment Applications. *J. Cleaner Prod.* **2018**, *182*, 8−15.
(15) Bailey, S. E.; Olin, T. J.; Bricka, R. M.; Adrian, D. D. A Review of Potentially Low-Cost Sorbents for Heavy Metals. *Water Res.* **1999**, *33*, 2469−2479.
(16) Blanchard, G.; Maunaye, M.; Martin, G. Removal of Heavy Metals from Waters by Means of Natural Zeolites. *Water Res.* **1984**, *18*, 1501−1507.
(17) Ahmed, W.; Mehmood, S.; Núñez-Delgado, A.; Ali, S.; Qaswar, M.; Shakoor, A.; Mahmood, M.; Chen, D.-Y. Enhanced Adsorption of Aqueous Pb(II) by Modified Biochar Produced through Pyrolysis of Watermelon Seeds. *Sci. Total Environ.* **2021**, *784*, 147136.

(18) Mahar, F. K.; He, L.; Wei, K.; Mehdi, M.; Zhu, M.; Gu, J.; Zhang, K.; Khatri, Z.; Kim, I. Rapid Adsorption of Lead Ions Using Porous Carbon Nanofibers. *Chemosphere* **2019**, *225*, 360−367.
(19) Fu, F.; Wang, Q. Removal of Heavy Metal Ions from Wastewaters: A Review. *J. Environ. Manage.* **2011**, *92*, 407−418.
(20) Carolin, C. F.; Kumar, P. S.; Saravanan, A.; Joshiba, G. J.; Naushad, M. Efficient Techniques for the Removal of Toxic Heavy Metals from Aquatic Environment: A Review. *J. Environ. Chem. Eng.* **2017**, *5*, 2782−2799.
(21) Bolisetty, S.; Peydayesh, M.; Mezzenga, R. Sustainable Technologies for Water Purification from Heavy Metals: Review and Analysis. *Chem. Soc. Rev.* **2019**, *48*, 463−487.
(22) Elimelech, M.; Phillip, W. A. The Future of Seawater Desalination: Energy, Technology, and the Environment. *Science* **2011**, *333*, 712−717.
(23) Baker, R. W. *Membrane Technology and Applications*; Wiley, 2012.
(24) Gin, D. L.; Noble, R. D. Designing the Next Generation of Chemical Separation Membranes. *Science* **2011**, *332*, 674−676.
(25) Werber, J. R.; Osuji, C. O.; Elimelech, M. Materials for Next-Generation Desalination and Water Purification Membranes. *Nat. Rev. Mater.* **2016**, *1* (5), 16018.
(26) Santhosh, C.; Velmurugan, V.; Jacob, G.; Jeong, S. K.; Grace, A. N.; Bhatnagar, A. Role of Nanomaterials in Water Treatment Applications: A Review. *Chem. Eng. J.* **2016**, *306*, 1116−1137.
(27) Ali, S.; Rehman, S. A. U.; Shah, I. A.; Farid, M. U.; An, A. K.; Huang, H. Efficient Removal of Zinc from Water and Wastewater Effluents by Hydroxylated and Carboxylated Carbon Nanotube Membranes: Behaviors and Mechanisms of Dynamic Filtration. *J. Hazard. Mater.* **2019**, *365*, 64−73.
(28) Yin, J.; Deng, B. Polymer-Matrix Nanocomposite Membranes for Water Treatment. *J. Membr. Sci.* **2015**, *479*, 256−275.
(29) Yang, Z.; Sun, P.-F.; Li, X.; Gan, B.; Wang, L.; Song, X.; Park, H.-D.; Tang, C. Y. A Critical Review on Thin-Film Nanocomposite Membranes with Interlayered Structure: Mechanisms, Recent Developments, and Environmental Applications. *Environ. Sci. Technol.* **2020**, *54*, 15563−15583.
(30) Guillen, G. R.; Pan, Y.; Li, M.; Hoek, E. M. V. Preparation and Characterization of Membranes Formed by Nonsolvent Induced Phase Separation: A Review. *Ind. Eng. Chem. Res.* **2011**, *50*, 3798−3817.
(31) Furukawa, H.; Cordova, K. E.; O'Keeffe, M.; Yaghi, O. M. The Chemistry and Applications of Metal-Organic Frameworks. *Science* **2013**, *341* (6149), 974.
(32) Li, W.; Zhang, Y.; Li, Q.; Zhang, G. Metal−organic Framework Composite Membranes: Synthesis and Separation Applications. *Chem. Eng. Sci.* **2015**, *135*, 232−257.
(33) Denny, M. S.; Kalaj, M.; Bentz, K. C.; Cohen, S. M. Multicomponent Metal−Organic Framework Membranes for Advanced Functional Composites. *Chem. Sci.* **2018**, *9*, 8842−8849.
(34) Li, X.; Wang, B.; Cao, Y.; Zhao, S.; Wang, H.; Feng, X.; Zhou, J.; Ma, X. Water Contaminant Elimination Based on Metal−Organic Frameworks and Perspective on Their Industrial Applications. *ACS Sustainable Chem. Eng.* **2019**, *7*, 4548−4563.
(35) Li, J.; Wang, H.; Yuan, X.; Zhang, J.; Chew, J. W. Metal-Organic Framework Membranes for Wastewater Treatment and Water Regeneration. *Coord. Chem. Rev.* **2020**, *404*, 213116.
(36) Tiburcio, E.; Greco, R.; Mon, M.; Ballesteros-Soberanas, J.; Ferrando-Soria, J.; López-Haro, M.; Hernández-Garrido, J. C.; Oliver-Meseguer, J.; Marini, C.; Boronat, M.; et al. Soluble/MOF-Supported Palladium Single Atoms Catalyze the Ligand-, Additive-, and Solvent-Free Aerobic Oxidation of Benzyl Alcohols to Benzoic Acids. *J. Am. Chem. Soc.* **2021**, *143*, 2581−2592.
(37) Bruno, R.; Mon, M.; Escamilla, P.; Ferrando-Soria, J.; Esposito, E.; Fuoco, A.; Monteleone, M.; Jansen, J. C.; Elliani, R.; Tagarelli, A.; et al. Bioinspired Metal-Organic Frameworks in Mixed Matrix Membranes for Efficient Static/Dynamic Removal of Mercury from Water. *Adv. Funct. Mater.* **2021**, *31* (6), 2008499.
(38) Mon, M.; Lloret, F.; Ferrando-Soria, J.; Martí-Gastaldo, C.; Armentano, D.; Pardo, E. Selective and Efficient Removal of Mercury from Aqueous Media with the Highly Flexible Arms of a BioMOF. *Angew. Chem., Int. Ed.* **2016**, *55*, 11167−11172.
(39) Mon, M.; Ferrando-Soria, J.; Grancha, T.; Fortea-Pérez, F. R.; Gascon, J.; Leyva-Pérez, A.; Armentano, D.; Pardo, E. Selective Gold Recovery and Catalysis in a Highly Flexible Methionine-Decorated Metal−Organic Framework. *J. Am. Chem. Soc.* **2016**, *138*, 7864−7867.
(40) Negro, C.; Martínez Pérez-Cejuela, H.; Simó-Alfonso, E. F.; Iqbal, W.; Herrero-Martínez, J. M.; Armentano, D.; Ferrando-Soria, J.; Pardo, E. (Multivariate)-Metal−Organic Framework for Highly Efficient Antibiotic Capture from Aquatic Environmental Matrices. *ACS Appl. Mater. Interfaces* **2023**, *15*, 3069−3076.
(41) Negro, C.; Escamilla, P.; Bruno, R.; Ferrando-Soria, J.; Armentano, D.; Pardo, E. Metal-Organic Frameworks as Unique Platforms to Gain Insight of Σ-Hole Interactions for the Removal of Organic Dyes from Aquatic Ecosystems. *Chem. —Eur. J.* **2022**, *28*, No. e202200034.
(42) Negro, C.; Martínez Pérez-Cejuela, H.; Simó-Alfonso, E. F.; Herrero-Martínez, J. M.; Bruno, R.; Armentano, D.; Ferrando-Soria, J.; Pardo, E. Highly Efficient Removal of Neonicotinoid Insecticides by Thioether-Based (Multivariate) Metal−Organic Frameworks. *ACS Appl. Mater. Interfaces* **2021**, *13*, 28424−28432.
(43) Mon, M.; Bruno, R.; Tiburcio, E.; Viciano-Chumillas, M.; Kalinke, L. H. G.; Ferrando-Soria, J.; Armentano, D.; Pardo, E. Multivariate Metal−Organic Frameworks for the Simultaneous Capture of Organic and Inorganic Contaminants from Water. *J. Am. Chem. Soc.* **2019**, *141*, 13601−13609.
(44) Escamilla, P.; Bartella, L.; Sanz-Navarro, S.; Percoco, R. M.; Di Donna, L.; Prejanò, M.; Marino, T.; Ferrando-Soria, J.; Armentano, D.; Leyva-Pérez, A.; et al. Degradation of Penicillinic Antibiotics and B-Lactamase Enzymatic Catalysis in a Biomimetic Zn-Based Metal−Organic Framework. *Chem. —Eur. J.* **2023**, *29*, No. e202301325.
(45) Bilanin, C.; Escamilla, P.; Ferrando-Soria, J.; Leyva-Pérez, A.; Armentano, D.; Pardo, E. Selective Cycloaddition of Ethylene Oxide to CO2 within the Confined Space of an Amino Acid-Based Metal−Organic Framework. *Dalton Trans.* **2023**, *52*, 18018−18026.
(46) Evans, P. Scaling and Assessment of Data Quality. *Acta Crystallogr., Sect. D: Biol. Crystallogr.* **2006**, *62*, 72−82.
(47) Evans, P. R.; Murshudov, G. N. How Good Are My Data and What Is the Resolution? *Acta Crystallogr., Sect. D: Biol. Crystallogr.* **2013**, *69*, 1204−1214.
(48) Winn, M. D.; Ballard, C. C.; Cowtan, K. D.; Dodson, E. J.; Emsley, P.; Evans, P. R.; Keegan, R. M.; Krissinel, E. B.; Leslie, A. G. W.; McCoy, A.; et al. Overview of the CCP 4 Suite and Current Developments. *Acta Crystallogr., Sect. D: Biol. Crystallogr.* **2011**, *67*, 235−242.
(49) Winter, G. Xia2: An Expert System for Macromolecular Crystallography Data Reduction. *J. Appl. Crystallogr.* **2010**, *43*, 186−190.
(50) Winter, G.; Waterman, D. G.; Parkhurst, J. M.; Brewster, A. S.; Gildea, R. J.; Gerstel, M.; Fuentes-Montero, L.; Vollmar, M.; Michels-Clark, T.; Young, I. D.; et al. DIALS: Implementation and Evaluation of a New Integration Package. *Acta Crystallogr., Sect. D: Struct. Biol.* **2018**, *74*, 85−97.
(51) Sheldrick, G. M. *SADABS Program for Absorption Correction, version 2.10*; Bruker Analytical X-ray Systems: Madison, WI, 2003, Analytical X-ray Systems, Madison, WI.
(52) Sheldrick, G. M. A Short History of SHELX. *Acta Crystallogr. A* **2008**, *64*, 112−122.
(53) Sheldrick, G. M. Crystal Structure Refinement with SHELXL. *Acta Crystallogr., Sect. C: Struct. Chem.* **2015**, *71*, 3−8.
(54) Parsons, S.; Flack, H. D.; Wagner, T. Use of Intensity Quotients and Differences in Absolute Structure Refinement. *Acta Crystallogr., Sect. B: Struct. Sci., Cryst. Eng. Mater.* **2013**, *69*, 249−259.
(55) Farrugia, L. J. WinGX Suite for Small-Molecule Single-Crystal Crystallography. *J. Appl. Crystallogr.* **1999**, *32*, 837−838.
(56) Farrugia, L. J. WinGX and ORTEP for Windows: An Update. *J. Appl. Crystallogr.* **2012**, *45*, 849−854.

https://doi.org/10.1021/acsami.4c12363
ACS Appl. Mater. Interfaces 2024, 16, 51182−51194

(57) Palmer, D. *CRYSTAL MAKER*; Cambridge University Technical Services: Cambridge, 1996.
(58) Velempini, T.; Pillay, K. Sulphur Functionalized Materials for Hg(II) Adsorption: A Review. *J. Environ. Chem. Eng.* **2019**, *7*, 103350.
(59) Sigel, R. K. O.; Skilandat, M.; Sigel, A.; Operschall, B. P.; Sigel, H. Complex formation of cadmium with sugar residues, nucleobases, phosphates, nucleotides, and nucleic acids. *Cadmium: from Toxicity to Essentiality. Metal Ions in Life Sciences*; Sigel, A.; Sigel, H.; Sigel, R., Eds.; Springer; Dordrecht, 2013, *11*, 191, 274, .
(60) Sigel, A.; Operschall, B. P.; Sigel, H. 11. Complex Formation of Lead(II) with Nucleotides and Their Constituents. In *Lead − Its Effects on Environment and Health*; De Gruyter, 2017; pp. 319402.
(61) Shen, J.; Ren, C.; Zeng, H. Surprisingly High Selectivity and High Affinity in Mercury Recognition by H-Bonded Cavity-Containing Aromatic Foldarands. *J. Am. Chem. Soc.* **2017**, *139*, 5387−5396.
(62) Scharnagl, N.; Buschatz, H. Polyacrylonitrile (PAN) Membranes for Ultra- and Microfiltration. *Desalination* **2001**, *139*, 191−198.
(63) Rouquerolt, J.; Avnir, D.; Fairbridge, C. W.; Everett, D. H.; Haynes, J. H.; Pernicone, N.; Ramsay, J. D. F.; Sing, K. S. W.; Unger, K. K. Recommendations for the Characterization of Porous Solids. *Pure Appl. Chem.* **1994**, *66*, 1739−1758.
(64) Cheng, L. S.; Yang, R. T. Improved Horvath—Kawazoe Equations Including Spherical Pore Models for Calculating Micropore Size Distribution. *Chem. Eng. Sci.* **1994**, *49*, 2599−2609.
(65) Mon, M.; Rivero-Crespo, M. A.; Ferrando-Soria, J.; Vidal-Moya, A.; Boronat, M.; Leyva-Pérez, A.; Corma, A.; Hernández-Garrido, J. C.; López-Haro, M.; Calvino, J. J.; et al. Synthesis of Densely Packaged, Ultrasmall Pt^0_2 Clusters within a Thioether-Functionalized MOF: Catalytic Activity in Industrial Reactions at Low Temperature. *Angew. Chem., Int. Ed.* **2018**, *57*, 6186−6191.
(66) Baratta, M.; Mastropietro, T. F.; Bruno, R.; Tursi, A.; Negro, C.; Ferrando-Soria, J.; Mashin, A. I.; Nezhdanov, A.; Nicoletta, F. P.; De Filpo, G.; et al. Multivariate Metal−Organic Framework/Single-Walled Carbon Nanotube Buckypaper for Selective Lead Decontamination. *ACS Appl. Nano Mater.* **2022**, *5*, 5223−5233.
(67) Lim, J. W.; Lee, J.-M.; Yun, S.-M.; Park, B.-J.; Lee, Y.-S. Hydrophilic Modification of Polyacrylonitrile Membranes by Oxyfluorination. *J. Ind. Eng. Chem.* **2009**, *15*, 876−882.
(68) Hansen, C. M. 50 Years with Solubility Parameters—Past and Future. *Prog. Org. Coat.* **2004**, *51*, 77−84.
(69) Chakrabarty, B.; Ghoshal, A. K.; Purkait, M. K. Preparation, Characterization and Performance Studies of Polysulfone Membranes Using PVP as an Additive. *J. Membr. Sci.* **2008**, *315*, 36−47.
(70) Tasselli, F.; Jansen, J.; Sidari, F.; Drioli, E. Morphology and Transport Property Control of Modified Poly(Ether Ether Ketone) (PEEKWC) Hollow Fiber Membranes Prepared from PEEKWC/PVP Blends: Influence of the Relative Humidity in the Air Gap. *J. Membr. Sci.* **2005**, *255*, 13−22.
(71) Yong, S. K.; Hyo, J. K.; Un, Y. K. Asymmetric Membrane Formation via Immersion Precipitation Method. I. Kinetic Effect. *J. Membr. Sci.* **1991**, *60*, 219−232.
(72) Chen, L.-W.; Young, T.-H. Effect of Nonsolvents on the Mechanism of Wet-Casting Membrane Formation from EVAL Copolymers. *J. Membr. Sci.* **1991**, *59*, 15−26.
(73) Friebe, S.; Mundstock, A.; Volgmann, K.; Caro, J. On the Better Understanding of the Surprisingly High Performance of Metal−Organic Framework-Based Mixed-Matrix Membranes Using the Example of UiO-66 and Matrimid. *ACS Appl. Mater. Interfaces* **2017**, *9*, 41553−41558.
(74) Jamshidifard, S.; Koushkbaghi, S.; Hosseini, S.; Rezaei, S.; Karamipour, A.; Jafari Rad, A.; Irani, M. Incorporation of UiO-66-NH2MOF into the PAN/Chitosan Nanofibers for Adsorption and Membrane Filtration of Pb(II), Cd(II) and Cr(VI) Ions from Aqueous Solutions. *J. Hazard. Mater.* **2019**, *368*, 10−20.
(75) Khosravi, A.; Habibpour, R.; Ranjbar, M. Enhanced Adsorption and Removal of Cd(II) from Aqueous Solution by Amino-Functionalized ZIF-8. *Sci. Rep.* **2024**, *14* (1), 10736.
(76) Cao, Y.; Du, M.; Han, F.; Luo, X.; Yang, W.; Lin, W.; Wang, Y.; Tang, W.; Li, Z. Carboxymethyl Cellulose Aerogel Decorated MOF-808 with Defects via Mixed-Metallic Center and Etching for Enhanced Pb(II) Removal. *Sep. Purif. Technol.* **2024**, *344*, 127262.
(77) Abedi, F.; Dubé, M. A.; Kruczek, B. Adsorption of Heavy Metals on the Surface of Nanofiltration Membranes: "A Curse or Blessing"? *J. Membr. Sci.* **2023**, *685*, 121988.

https://doi.org/10.1021/acsami.4c12363
ACS Appl. Mater. Interfaces 2024, 16, 51182−51194